metals

MDPI

Article

Numerical Simulation on the Origin of Solidification Cracking in Laser Welded Thick-Walled Structures

Nasim Bakir [1,2,*], Antoni Artinov [1], Andrey Gumenyuk [1], Marcel Bachmann [1] and Michael Rethmeier [1,2]

[1] BAM Federal Institute for Material Research and Testing, 12205 Berlin, Germany; antoni.artinov@bam.de (A.A.); andrey.gumenyuk@bam.de (A.G.); marcel.bachmann@bam.de (M.B.); michael.rethmeier@bam.de (M.R.)

[2] Department of Joining Technology, Technische Universität Berlin, 10623 Berlin, Germany

* Correspondence: nasim.bakir@bam.de; Tel.: +49-30-8104-4622

Received: 17 May 2018; Accepted: 29 May 2018; Published: 1 June 2018

Abstract: One of the main factors affecting the use of lasers in the industry for welding thick structures is the process accompanying solidification cracks. These cracks mostly occurring along the welding direction in the welding center, and strongly affect the safety of the welded components. In the present study, to obtain a better understanding of the relation between the weld pool geometry, the stress distribution and the solidification cracking, a three-dimensional computational fluid dynamic (CFD) model was combined with a thermo-mechanical model. The CFD model was employed to analyze the flow of the molten metal in the weld pool during the laser beam welding process. The weld pool geometry estimated from the CFD model was used as a heat source in the thermal model to calculate the temperature field and the stress development and distributions. The CFD results showed a bulging region in the middle depth of the weld and two narrowing areas separating the bulging region from the top and bottom surface. The thermo-mechanical simulations showed a concentration of tension stresses, transversally and vertically, directly after the solidification during cooling in the region of the solidification cracking.

Keywords: laser beam welding; solidification cracking; numerical simulation; CFD model; finite element method (FEM); weld pool; full penetration

1. Introduction

For several years, solid-state lasers have been widely applied in metal processing. The high-power of the laser sources and the excellent beam quality allow structures with wall thicknesses of more than 10 mm to be welded in one pass. The high welding speed, low heat input, and low-distortion of the laser beam welding are all advantages that significantly contribute to increasing productivity during the fabrication of thick-walled constructions, and reducing rework [1]. However, when using the laser to weld steels with thickness above 10 mm, the risk of solidification cracking of materials increases due to carelessly coordinated process parameters and mechanical conditions.

Due to the complex nature of the hot cracking phenomena, many hypotheses and theories have been presented in the past decades. Apblett and Pellini [2] assumed that solidification cracking first occurs due to a critical strain. They believed that hot cracks occur at a temperature slightly above the solidus temperature when a film of liquid is still present between the dendrite structures. The hot cracks appear when the highly localized strains in the liquid films exceed their critical limit. Prokhorov [3–5] suggested that the materials show a reduced deformation capacity in a specific temperature range, known as the Brittle Temperature Range (BTR). If the strain during solidification exceeds the deformation capacity, hot cracks will occur.

According to in situ observations of crack formation and numerical simulations, an approach describing the functional relationship between the resulting stresses in the weld and the hot cracking formation was presented by Zacharia et al. [6,7]. The researchers indicated that the transverse compressive stress immediately behind the pool prevents the formation of hot cracks. The hot cracks will form if a liquid film is present behind the weld pool, such as when the transverse stress changes from compressive to tensile within the mushy zone (see Figure 1).

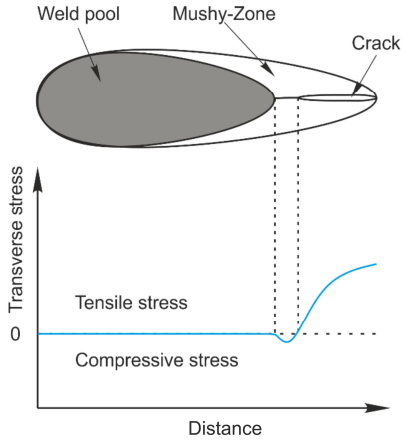

Figure 1. Representation of the influence of the transverse stress development on the hot cracking, according to [6].

Feurer [8] introduced a metallurgical model in which the ratio of the cooling-related volume deformation, the so-called rate of shrinkage (ROS), and the rate of feeding (ROF) for closing the cavity are considered. According to this theory, the critical point will be reached when ROF and ROS are equal. In this condition, hot cracks can be avoided. In the case of a higher shrinkage than feeding rate, hot cracks will occur.

In welding of thick-walled structures, the problematic solidification cracking becomes even more complicated. Because of the complex weld pool shape, which is affected by the penetration depth, its solidification behavior plays an additional role in the hot cracking phenomena.

Shida et al. [9] observed the change in the weld pool geometry, depending on penetration depth. In their observations, they found a correlation between the weld pool shape and the solidification cracking by studying the effect of the welding parameter of electron beam welding (EBW) on the weld pool shape. However, it was reported that a small cavity in the rear part of the weld pool at approximately one half of the penetration depth resulted from a certain focus position of the electron beam. The observed cavity has been shown to have a significant influence on solidification cracking.

Locally delayed solidification in the electron beam welding was studied by Tsukamoto et al. in [10,11]. A connection between the delay in the solidification, the formation of the solidification cracking, and the porosity was identified.

Gebhardt et al. [12,13] observed the same phenomena in laser beam welding for thick-walled structures, with the outcome being called bulging in the weld. Their numerical simulations showed that the bulging has a significant influence on the temperature field and mechanical stress distribution, which contributes to the formation of hot cracking.

Barbetta et al. [14] confirmed a high correlation between the bulging in the weld and the occurrence of solidification cracks, as the solidification crack is always associated with a bulge. These phenomena, bulging and hot cracking, are related by the delayed solidification at the rear part of the weld pool.

Schaefer et al. [15] reduced the hot cracks formation in steel by modulation with laser power. However, additional investigation is still needed to clarify the interaction between the weld pool geometry, the thermally induced tensile stresses, and the strain in the weld zone.

The aim of this study is to use a computational fluid dynamic (CFD) simulation for investigation and analysis of the weld pool shape for low-alloyed structural steel with a thickness of 12 mm to observe the thermally deduced stresses by using a thermo-mechanical model in the weld zone and analyze its influence on the solidification cracking.

2. Materials and Methods

Low-alloyed steel plates (S355-EN 10025) with 12 mm thickness were used in the welding experiments. The chemical composition of the steel and the process parameters are listed in Tables 1 and 2, respectively. The joint partners were clamped to a device with known restraint intensity (see Figure 2).

Table 1. Chemical composition (in wt. %).

C	Si	Mn	P	S	Cr	Cu	Mo	Fe
0.088	0.34	1.38	0.011	0.002	0.048	0.020	0.007	Bal.

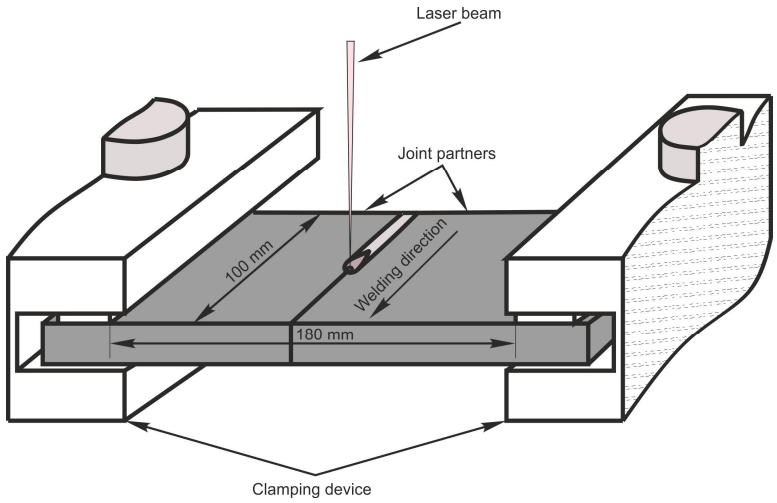

Figure 2. Schematic illustration of the experiments.

The concept of the intensity of restraint has been introduced by [16,17]. This represents the stiffness of the surrounding structure around the weld and its influence on the stress development during solidification. The total restraint intensity of the presented experimental construction before welding was 12.6 kN/(mm·mm), estimated according to [18,19].

Table 2. Welding parameters used in the experiments.

Parameters	Value
Laser power	14 kW
Welding speed	2 m/min
Focal position	−2 mm
Weld seam length	100 mm
Plate thickness	12 mm
Shielding gas	N_2
Restraint intensity	12.6 kN/(mm·mm)

To study more deeply the effect of the weld pool shape on the temporal and spatial distribution of the stresses, the model was divided into three simulation phases:

- CFD model: Calculation of the heat and mass transport in the weld pool to analyze the weld pool shape.
- Thermal FEM model: The CFD-obtained weld pool geometry is used as a heat source in the calculation of the temperature field.
- Mechanical FEM model: Using the calculated transient temperature field as a thermal load in the mechanical model to evaluate the stress field.

2.1. CFD Model

The proposed mathematical model in this paper was implemented and solved with the commercial Software ANSYS Fluent (ANSYS Inc., Canonsburg, PA, USA). In addition, the CFD simulation of full-penetration keyhole laser beam welding was used to obtain the weld pool geometry by considering the most relevant physical effects, such as Marangoni and natural convection, fusion heat and temperature-dependent material properties up to evaporation temperature. The geometrical dimensions of the computational domain were 40 mm × 25 mm × 12 mm (see Figure 3b). A symmetry plane was applied to reduce the numerical effort and computational time while the computational domain was discretized by a polygonal mesh of tetrahedral elements. The total number of mesh elements was about 9×10^5 (see Figure 3b), allowing for a minimum element size of 0.08 mm at the free surfaces and the keyhole wall to be used. Because the physical phenomena behind the laser beam welding process are strongly coupled and temperature dependent, a highly nonlinear system of equations must be solved to obtain a solution.

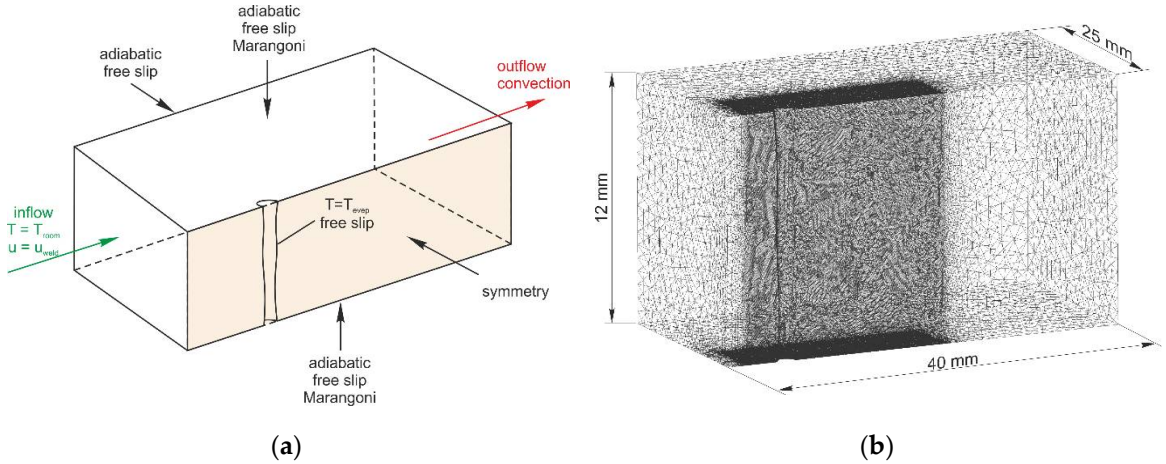

(**a**) (**b**)

Figure 3. (**a**) Boundary condition of the computational fluid dynamic (CFD) model according to [20,21]. (**b**) The model after meshing.

Here, a simplified form of the numerical model was used to guarantee numerical stability and reasonable computing time. The main assumptions in the model were similar to those used in [22], and are given as follows:

- Transient approach until reaching a quasi-steady-state.
- Adapted size of the computational domain.
- Fixed free surface geometry.
- Approximated simplified and fixed keyhole geometry from the weld cross-section (see Figure 4), used as a model parameter to adapt the numerical to the experimental results. Thus, effects caused by keyhole oscillations were not considered.
- Shear stress due to the interaction of metal vapor and liquid metal was not considered.
- Heat losses by radiation were neglected due to the high relation of volume versus surface of the plate.

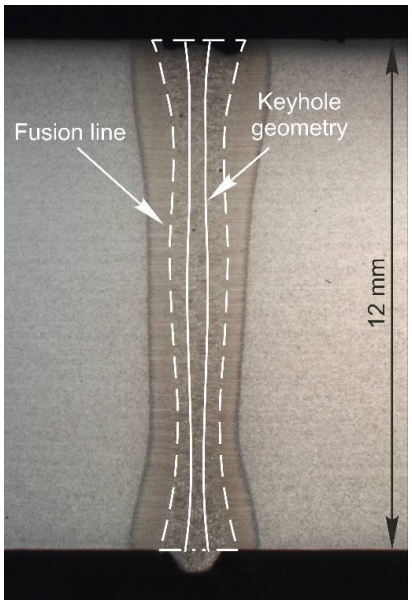

Figure 4. Cross-section of the weld and the used keyhole geometry in the CFD model.

The thermophysical properties of the low-alloyed steel used for the calculation can be taken from [23]. The velocity, pressure and temperature fields of the incompressible flow were approximated by the numerical solution of the mass, the momentum and the energy conservation equations by making use of the simulation framework of ANSYS Fluent. The numerical setup including the geometry of the workpiece, the initial state, and the boundary conditions can be seen in Figure 3a. Note, the heat input was considered as a boundary condition at the keyhole surface by setting the temperature there equal to evaporation temperature. A turbulent flow pattern, based on the high velocities on both upper and lower sides—caused by the Marangoni-driven flow—and the influence of the keyhole geometry on the flow, was considered by combining the Reynolds-Averaged-Navier–Stokes (RANS) equations with the κ-ε turbulence model. Natural convection and buoyancy-driven flows due to gravity were considered by the Boussinesq approximation and the enthalpy-porosity technique was applied to simulate the solid-liquid phase transformation. The heat conductivity was modified by the Kays and Crawford heat transport turbulence model and accounts for the amount of produced turbulent heat conductivity. To consider the latent heat of fusion by the solid-liquid and liquid-solid phase transformation, the method of apparent heat capacity was included.

2.2. Thermo-Mechanical Model

A plane strain two-dimensional model was employed to perform the thermo-mechanical simulation. All out-of-plane strain components were neglected. The thermo-physical material properties were taken from [22].

The stress-strain diagram was taken from the Sysweld material database (ESI Group, Paris, France) [23] and the data was supplied for S355J2G3. The material was assumed to follow an elasto-plastic law with isotropic hardening behaviour (von Mises plasticity model).

The phase transformation is also considered in the model. The material properties of all elements reaching the austenite end temperature (A_{C3}) changed during cooling to austenite. When austenite is cooled to the martensite finish temperature (M_F), the material properties of the elements changed to martensite. Elements that do not reach the austenite start temperature (A_{C1}) maintain the properties of the base material. Another material model was used for the element, which reaches a temperature above A_{C1} and below A_{C3}. This model was composed of 50% of base material and martensite properties below M_F and 50% of base material and austenite properties above M_F, until the martensite start temperature (M_S).

The clamping has been replaced in the model with one-dimensional spring elements that have similar stiffness. Figure 5 shows the dimensions and the applied boundary conditions used in the thermo-mechanical model. This simplification has been used in [24,25]. The Birth and Death feature has been used for all elements receiving an average temperature of 1440 °C. All these elements, reaching the melting temperature, were "killed". The stiffness matrix for these elements was multiplied by a penalty factor and all strains, including the plastic strains, were eliminated. The computed weld pool geometry from CFD simulation was used as a heat source to calculate the temperature field in the thermal model.

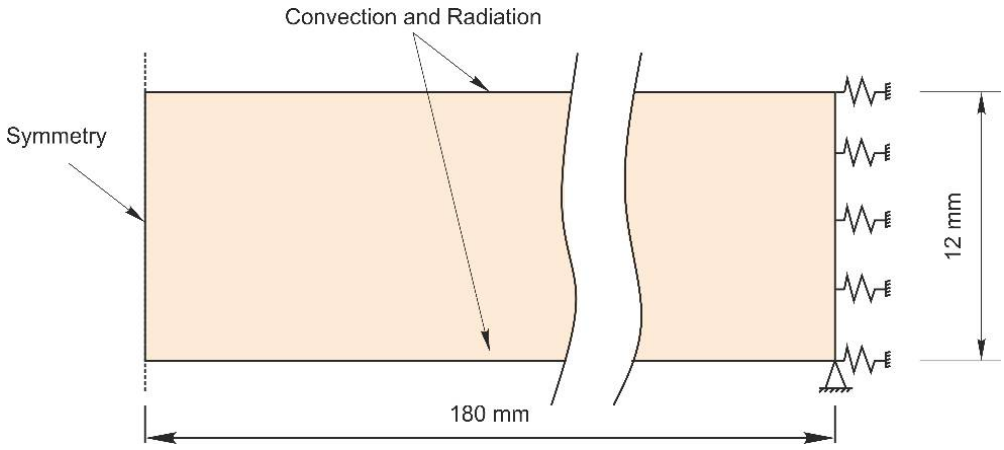

Figure 5. Boundary conditions used in the thermo-mechanical analysis.

3. Results and Discussion

Radiographic tests showed that cracks formed in the weld interior (see Figure 6a). In Figure 6b, a micrograph of the weld cross-section presents a typical vertical solidification crack in the weld centerline. It should be noted that small cracks that can be observed in the weld and the heat-affected zone were not taken into consideration in this study. Moreover, the low-alloyed steel was not susceptible to either liquation cracks or Ductility Dip Cracking (DDC), or cold cracks [26]. These findings are similar to those reported by [25], where they welded 15 mm plate under similar restraint conditions.

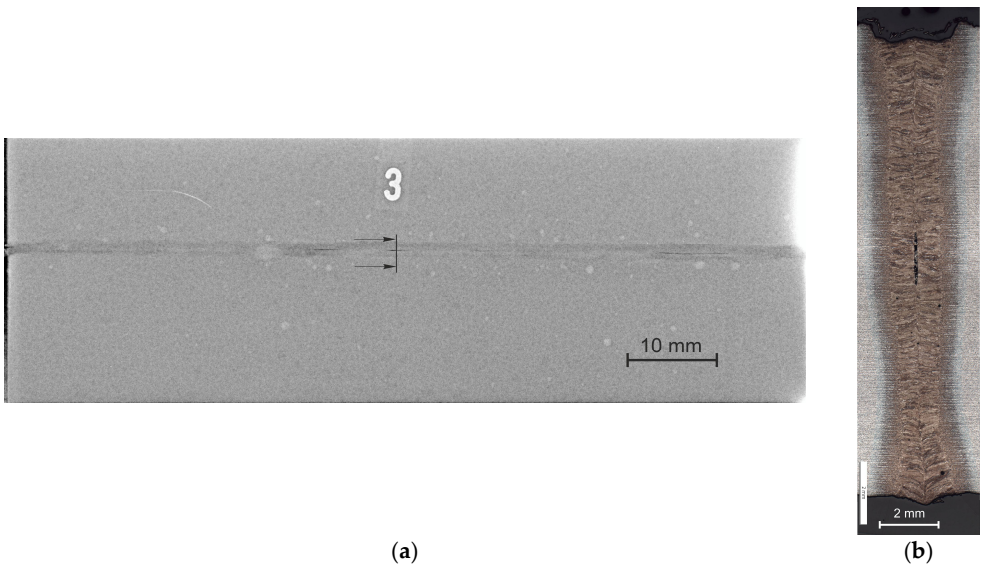

(**a**) (**b**)

Figure 6. (**a**) Radiographic film of a welded sample. (**b**) Weld cross-section at the crack location.

However, such cracks are related to a high weld depth-to-width ratio. This ratio leads to a pronounced intersection of columnar grains, along with a plane at the weld centerline and the accumulation of segregations in this zone. It is believed that if the weld metal is unable to accommodate the contractional strains of solidification and cooling, hot cracks will inevitably originate.

However, the experiments were conducted to create appropriate conditions for solidification cracking initiation. Those boundary conditions and the results of the crack location, as well as the cross-section and the temperature measurement were used for the calibration of the numerical models.

The aim of the CFD model was to predict the geometry of the quasi-steady-state weld pool in the stable zone of the weld. The three-dimensional weld pool geometry is defined by the liquidus temperature (see Figure 7a), and part of this isotherm can be seen in the symmetry plane of the CFD model (see Figure 7b). In Figure 7, three regions of the weld pool can be recognized. The weld pool shape is strongly influenced by the Marangoni convection in the upper and lower sides of the part. Together with the movement of the laser source, three regions are developed: an upper, a bulging (middle), and a lower region. The observed velocities of the melt in the bulging region were very small compared to the values in the upper and lower regions. Hence, the edge of the middle region is nearly a parallel shift of the keyhole edge, which forms together with the two backflows due to the thermo-capillary-driven flow the observed bulge.

The quasi-steady-state weld pool represents the state of a mass and energy equilibrium defined by the moving energy source and the solidification speed at the trailing part of the weld pool. Due to the movement of the energy source along the partly cold material, new material is melted and added to the weld pool. This is then transferred by the different flows in the molten pool. Simultaneously, through the heat transfer, the same amount of molten material solidifies at the trailing part of the weld. In the present model, the flows in the upper and lower regions dominate and transfer cooler material back to the vicinity of the keyhole, ensuring mass conservation. The two necking areas are formed and, consequently, also the bulge (see Figure 7).

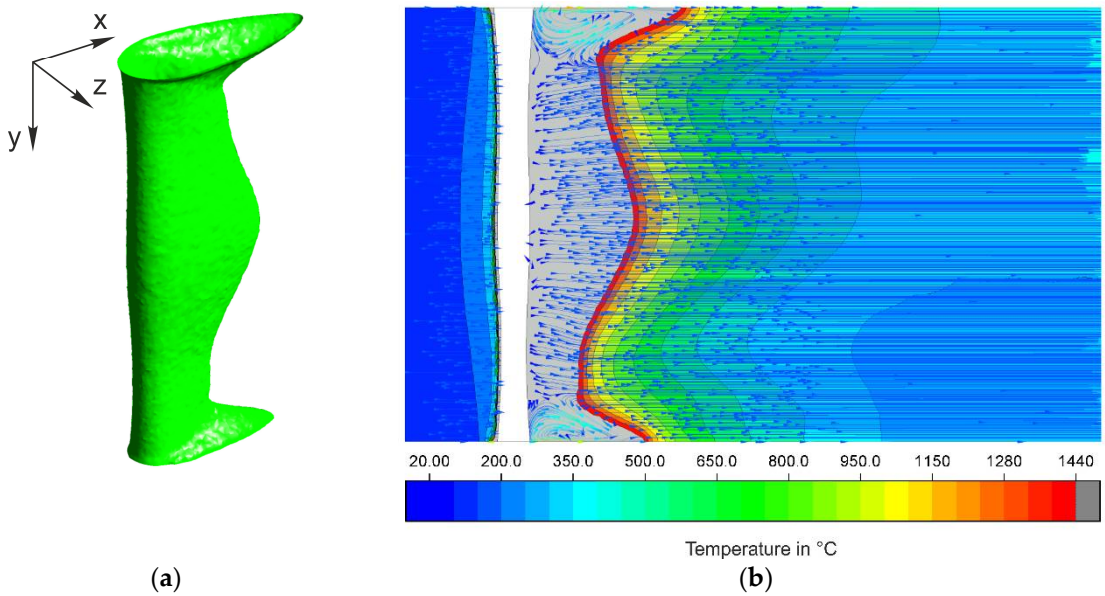

Figure 7. (**a**) The weld pool geometry defined by the liquidus temperature. (**b**) Temperature field and velocity streamlines in the symmetry plane of the model.

The diameter of the keyhole was used as a parameter to achieve a good match between the experiments and the model. This parameter was adjusted until an error of less than 5% was obtained. The fused zone, highlighted with dashed lines, agrees well with the experiment (see Figure 8).

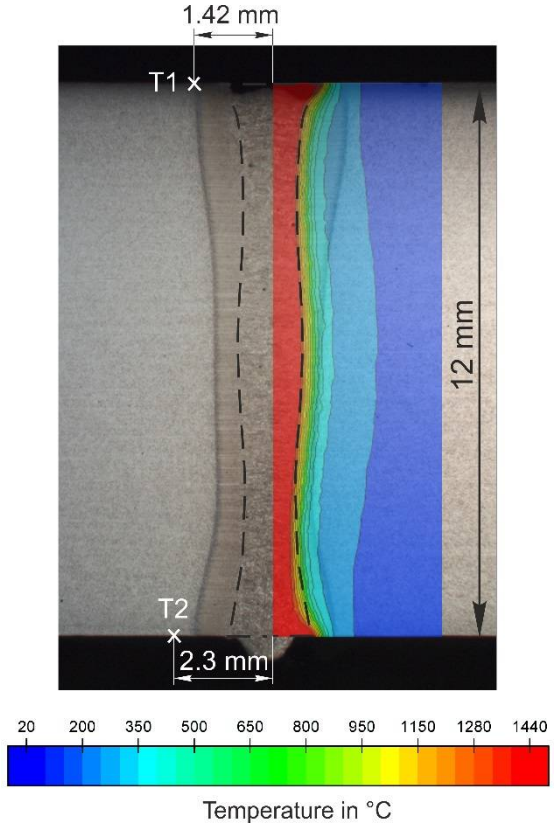

Figure 8. Comparison of the fused zone between experiment and CFD model.

Figure 9 shows the temperature measurements over time using thermocouples on the top and the bottom of the specimen surface compared to measurements obtained from calculations.

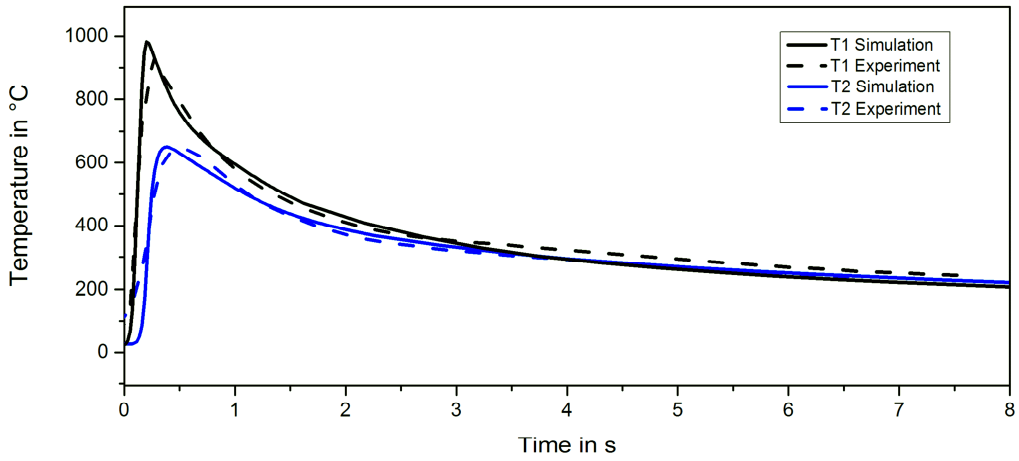

Figure 9. Comparison of the temperature measurements between experiments and the computational model.

To use the computed weld pool geometry as a heat source in the two-dimensional model, it was assumed that the temperature within the melt isotherm is homogeneous, constant, and equal to melting temperature (1440 °C). Then, the weld pool simply consists of multiple layers of two combined half-ellipses, as shown schematically in Figure 10.

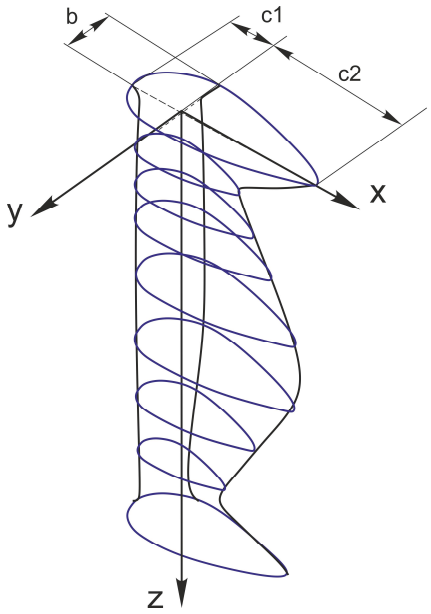

Figure 10. Schematic representation of the weld pool geometry and the parameters of two combined half-ellipses.

The equation of the combination of two half-ellipses can be given as flowing:

$$\frac{x^2}{c^2(x,z)} + \frac{y^2}{b^2(z)} = 1$$

where:

$$c(x,z) = \begin{cases} c = c1 \text{ if } x \leq 0 \\ c = c2 \text{ if } x > 0 \end{cases}$$

The front part of the combination of the ellipses is defined by parameters b and c1 and the rear of the ellipse is defined by b and $c2$. The parameter c is a function of the weld pool length (x-coordinate) and the weld pool depth (z-coordinate), and the parameter b is a function of the weld pool depth.

The parameters $c1$, $c2$, and b were fitted with fourth-degree polynomial function (see Figure 11). The obtained quartic functions were employed for the calculation of those parameters in the thermal model.

The developed heat source will check at each time step, whether the nodes are located inside one of the ellipses, and if so, the temperature will be changed to the melt temperature. If not, the temperature will be maintained.

Figure 12 shows a comparison of the temperature field between calculations, using the CFD model on the right and using the developed heat source, which was previously described, on the opposite side of the temperature field. A very slight difference can be observed between fusion lines. This difference is a result of the fitting of the heat source parameters. However, the results of this technique showed high efficiency in the transfer of computed weld pool geometry, which cannot be achieved by using common heat sources, such as the conical Gaussian heat source model [27], the cylindrical heat source model [28], or the combination of both [29,30].

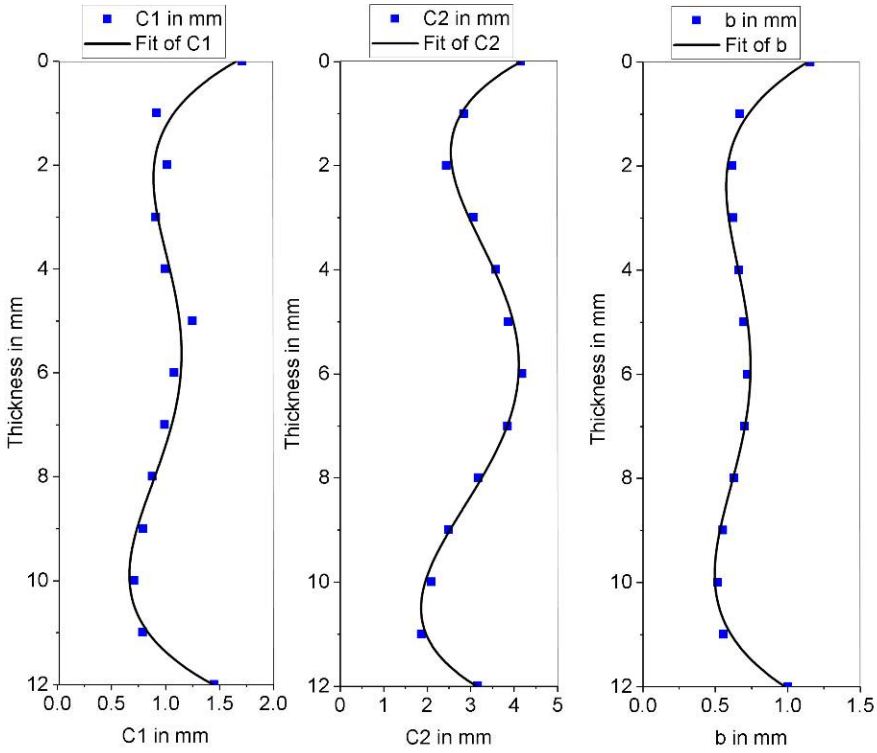

Figure 11. The fitting of the parameters $c1$, $c2$ and b as a function of the weld depth.

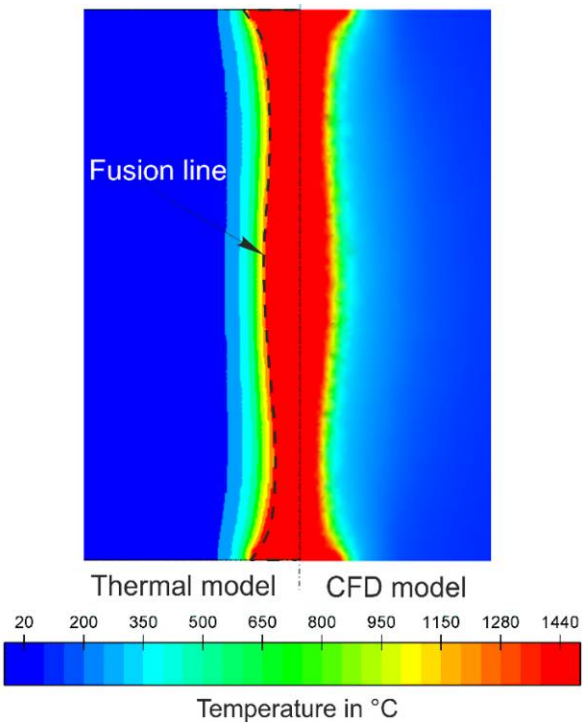

Figure 12. Comparison of the temperature fields of the CFD and the thermal model.

These heat source models were mainly developed based on the cross-section of the weld, without considering the weld pool in the longitudinal section. However, this fulfills the purpose of the calculation of residual stresses and the distortions.

The transversal stress distribution and the temperature distribution of approximately 230 ms after complete solidification of the melt (i.e., at 1100 °C in the middle of the weld) are shown in Figure 13. A concentration of the tensile stress can be observed in the middle of the weld in the bulging region. Regions subject to high compressive stresses can be observed at the top and bottom of this region. The same observation can be found for the vertical stress (see Figure 14).

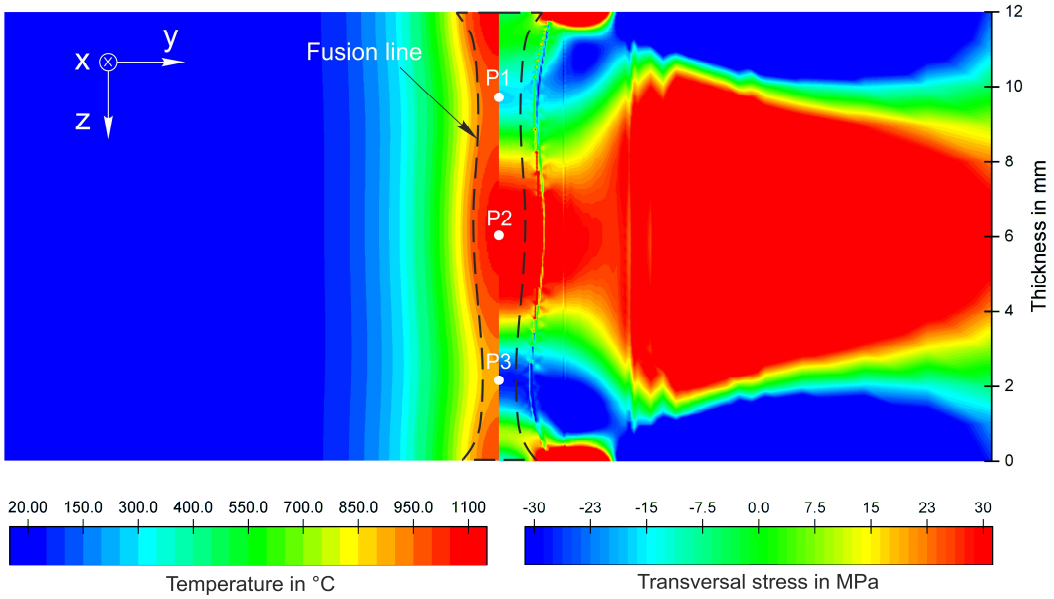

Figure 13. Transversal stress distribution and temperature distribution after solidification of the weld pool.

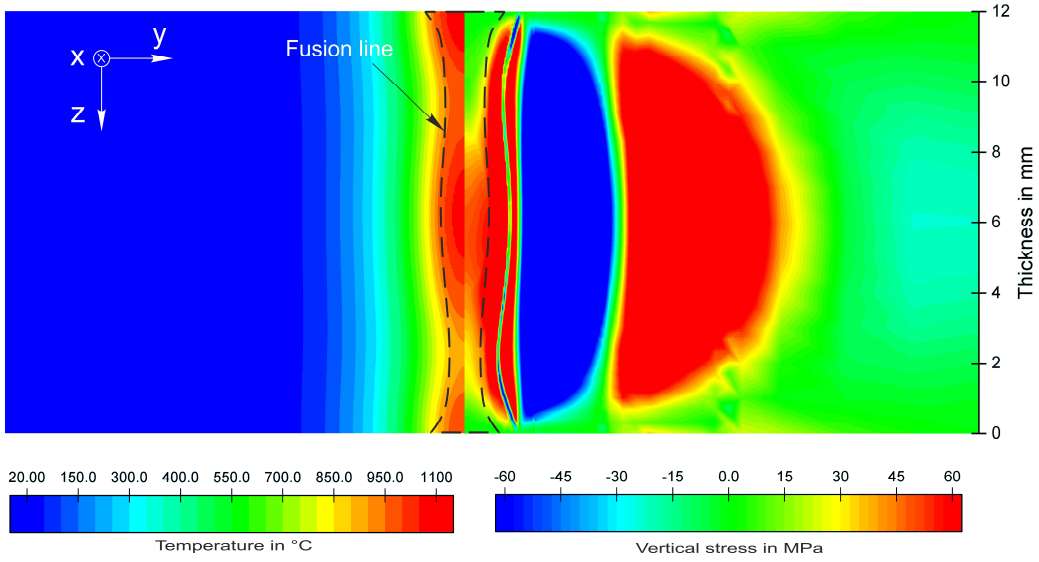

Figure 14. Vertical stress distribution and corresponding temperature distribution after solidification of the weld pool.

To closely evaluate the observed stress distribution at this moment, three evaluation points were chosen, which were positioned below each other. P1 represents the upper narrowing region, P2 the bulging region, and P3 the lower narrowing region (see Figure 13). Figures 15 and 16 indicate the transversal and vertical stress evolution versus the time during cooling at the locations P1, P2, and P3. On the narrowing regions (P1 and P3), the transversal stresses developed in a very similar manner

because immediately after solidification, tensile stresses appeared for a short period and soon became compressive stresses until reaching the value of −30 MPa. Nevertheless, the vertical stresses in all regions show tensile development.

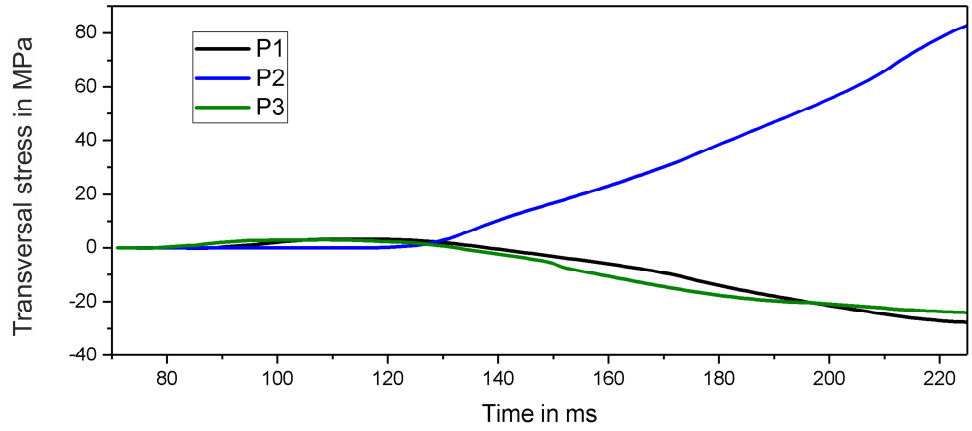

Figure 15. Transversal stress evaluation on the points P1, P2, and P3.

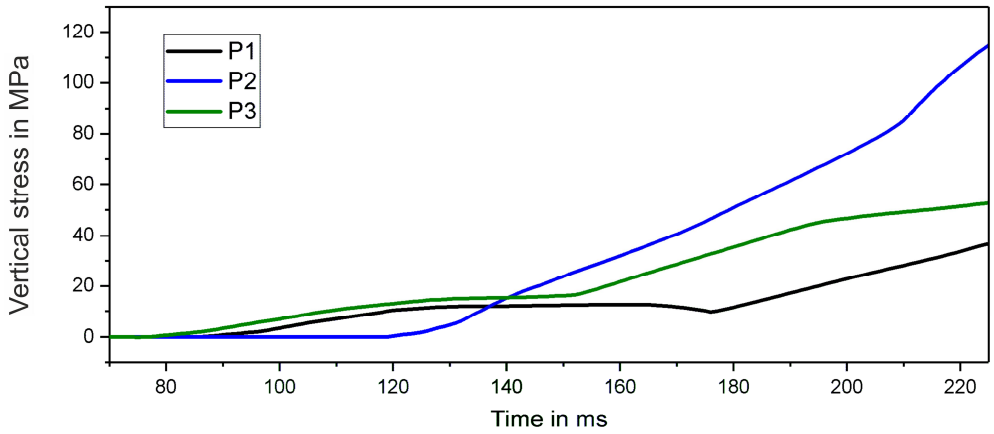

Figure 16. Vertical stress evaluation on the points P1, P2, and P3.

In the bulging region (P2), transversal and vertical tensile stresses development can be observed immediately after solidification, continuing to rise until reaching a value of 80 MPa and 110 MPa, respectively. The vertical tensile stress along the weld depth can be returned to the restraint of the plate to the vertical shrinkage of the weld. However, since the transversal stresses have an opposite direction to the dendrites growth, the stresses are held responsible for the formation of these cracks.

As previously observed, the chronological order of the solidification of the weld cannot be separated from the nature and distribution of the stresses in the weld zone. To explain this mutual interaction in the weld during cooling, Figure 17 schematically shows the melt and the solid distribution in a considered plane orthogonal to the welding direction, while the weld pool passes through it, at three consecutive moments of time. Moment T1 represents the section on the widest location of the weld pool crossing the plane. Until this moment, the weld region is heated from room temperature to melt temperature, and the weld volume expands. This expansion is restrained by the surrounding cold material, in addition to the restraint of the clamping causing compressive stress in the surrounding material. In this moment, no stresses have taken place in the weld zone because the melt has nil strength [2]. It must be noted that the stress resulting from the thermal strains during solidification is relieved as long as the connection to the melt is available.

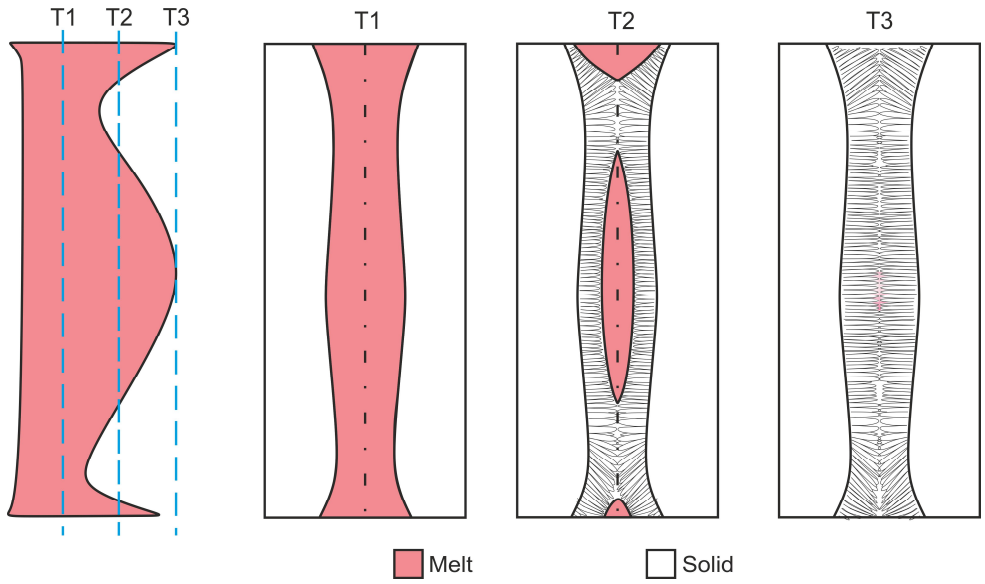

Figure 17. Schematic illustration of the distribution of the melt and solid in three points in time (T1, T2 and T3) during solidification of the weld pool.

As the weld pool moves slightly forward there are still melted regions within the bulging top and bottom parts, whereas the narrowing regions solidify between them (T2). As long as these liquid regions have access to the melt or to the top and bottom free surfaces, the resulting thermal stresses can be relieved. This corresponds to the observations at points P1 and P3.

At the last stage of solidification, corresponding to the time T3, the bulging region solidifies and the surrounding material is already in a solid state. Then the entire amount of stress resulting from the thermal strain adds to the stresses. At this moment, the dendrite arms have coalesced and feeding of the melt is difficult. When a melt film is still present between the two solidification fronts, due to the localization of high tensile stress, the initiation of solidification cracks is expected (see Figure 18). The risk of formation of the solidification cracks continues until the temperature reaches 988 °C, due to low melting phases such as Fe-S [31].

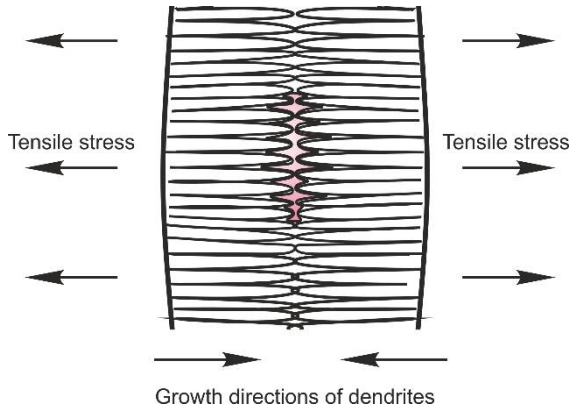

Figure 18. Schematic representation of solidification cracking in the bulging region.

4. Conclusions

In this study, a three-dimensional CFD-simulation model was developed to simulate the fluid flow in the weld pool. The CFD model showed a bulging region in the middle of the depth, which is separated from the top surface and bottom surface by two narrowing regions. It can be concluded

that the interaction of the movement of the laser source with the Marangoni vortex leads to a teardrop shape at the upper and bottom surface of the workpiece. Additionally, it shows that the bulging in the weld is a result of the backflows on the upper and lower sides due to the thermo-capillary-driven flows.

The weld pool shape was used as a heat source in a two-dimensional thermo-mechanical model, which allows a highly accurate transformation of the weld pool dimensions obtained from the CFD model. This developed technique allows the consideration of physical aspects, which cannot be considered when using traditional heat sources.

The mechanical model showed that the chronological order of the solidification of the weld has a significant influence on the nature and distribution of the stresses in the weld. High tensile stress has been observed in the bulging region, i.e., in the susceptible region for solidification cracking, when compared to the other narrowing regions, which show compressive stress.

Author Contributions: The numerical simulation models have been developed by N.B. and A.A. Discussion and conclusions have been written with the contribution of all authors.

Funding: This work was supported by the Research Association for Steel Application (FOSTA), the Federation of Industrial Research Associations (AiF) and the German Federal Ministry for Economic Affairs and Energy, (BMWi Bundesministerium für Wirtschaft und Energie), (Project 19582N, 'Investigation of the influence the restraint conditions on hot cracking in laser and laser-hybrid welding of thick structure steels'). Financial funding of the Deutsche Forschungsgemeinschaft (DFG, German Research Foundation) under Grant Nr. BA 5555/1-1 is gratefully acknowledged.

Conflicts of Interest: The authors declare no conflict of interest.

References

1. Kelly, S.M.; Brown, S.W.; Tressler, J.F.; Martukanitz, R.P.; Ludwig, M.J. Using hybrid laser-arc welding to reduce distortion in ship panels. *Weld. J.* **2009**, *88*, 32–36.
2. Apblett, W.R.; Pellini, W.S. Factors Which Influence Weld Hot Cacking. *Weld. Res. Suppl.* **1954**, *33*, 83–90.
3. Prokhorov, N.N. Resistance to hot tearing of cast metals during solidification. *Russ. Cast. Prod.* **1962**, *2*, 172–175.
4. Prokhorov, N.N. The problem of the strength of metals while solidifying during welding. *Svar. Proizv.* **1956**, *6*, 5–11.
5. Prokhorov, N.N. The Technological Strength of Metals while Crystallising during Welding. *Svar. Proizv.* **1962**, *4*, 1–8.
6. Zacharia, T. Dynamic Stresses in Weld Metal Hot Cracking. *Weld. Res. Suppl.* **1994**, *73*, 164–172.
7. Feng, Z.; David, S.A.; Zacharia, T.; Tsai, C.L. Quantification of Thermomechanical Conditions for Weld Solidification Cracking. *Sci. Technol. Weld. Join.* **1997**, *2*, 11–19. [CrossRef]
8. Feurer, U. Influence of alloy composition and solidification conditions on dendrite arm spacing, feeding and hot tearing properties of aluminium alloys. In Proceedings of the International Symposium on Engineering Alloys, Delft, The Netherlands, 3–4 March 1977; pp. 131–145.
9. Shida, T.; Okumura, H.; Kawada, Y. Effects of welding parameters and prevention of defects in deep penetration electron beam welding of heavy section steel plates. *Weld. World* **1979**, *17*, 196–207.
10. Tsukamoto, S.; Irie, H. Mechanism of locally delayed solidification in electron beam welding. *Weld. Int.* **1991**, *5*, 177–183. [CrossRef]
11. Tsukamoto, S.; Irie, H. Welding defects and molten metal behaviour in low speed electron beam welding. *Weld. World* **1985**, *23*, 130–140.
12. Gebhardt, M.O.; Gumenyuk, A.; Rethmeier, M. Solidification cracking in laser GMA hybrid welding of thick-walled parts. *Sci. Technol. Weld. Join.* **2014**, *19*, 209–213. [CrossRef]
13. Gebhardt, M.O.; Quiroz Penaranda, V.; Gumenyuk, A.; Rethmeier, M. Restraint effects on stresses and strains in single-run high power laser beam welding of thick plates. *Math. Model. Weld Phenom.* **2010**, *9*, 1011–1033.
14. Barbetta, L.D. *Solidification Flaw and Porosity Formation in Hybrid Laser: GMA Welding of Thick API 5L X70 Steel Plates*; Universidade Federal de Santa Catarina: Florianópolis, Brazil, 2014.
15. Schaefer, M.; Kessler, S.; Scheible, P.; Graf, T. Modulation of the laser power to prevent hot cracking during laser welding of tempered steel. *J. Laser Appl.* **2017**, *29*, 42008. [CrossRef]

16. Satoh, K.; Ueda, Y.; Kiharak, H. Recent trend of researches on restraint stresses and strains for weld cracking. *Trans. JWRI* **1972**, *42*, 53–68. [CrossRef]
17. Matsubuchi, K. *Analysis of Welded Structure*; Pergamon Press: Oxford, UK, 1980.
18. Wongpanya, P.; Boellinghaus, T. Residual Stress Distribution in Competing S 1100 QL Butt-Welds Dependent on Plate Thickness and Restraint Length. In Proceedings of the Conference on High Strenght Steels for Hydropower Plants, Takasaki, Japan, 20–22 July 2009; pp. 1–11.
19. Cross, C.E.; Böllinghaus, T. The Effect of Restraint on Weld Solidiflcation Cracking in Aluminium. *Weld. World* **2005**, *2*, 458–463.
20. Bachmann, M.; Avilov, V.; Gumenyuk, A.; Rethmeier, M. Numerical simulation of full-penetration laser beam welding of thick aluminium plates with inductive support. *J. Phys. D* **2011**, *45*, 35201. [CrossRef]
21. Bachmann, M.; Avilov, V.; Gumenyuk, A.; Rethmeier, M. About the influence of a steady magnetic field on weld pool dynamics in partial penetration high power laser beam welding of thick aluminium parts. *Int. J. Heat Mass Transf.* **2013**, *60*, 309–321. [CrossRef]
22. Artinov, A.; Bachmann, M.; Rethmeier, M. Equivalent heat source approach in a 3D transient heat transfer simulation of full-penetration high power laser beam welding of thick metal plates. *Int. J. Heat Mass Transf.* **2018**, *122*, 1003–1013. [CrossRef]
23. *Sysweld Material Database*; ESI Group: Paris, France, 2009.
24. Gebhardt, M.O.; Gumenyuk, A.; Rethmeier, M. Numerical analysis of hot cracking in laser-hybrid welded tubes. *Adv. Mater. Sci. Eng.* **2013**, *2013*, 1–8. [CrossRef]
25. Quiroz, V.; Gebhardt, M.; Gook, S. Hot cracking in high power laser beam welding of thick high strength structural steels under restraint conditions. In Proceedings of the ICALEO 2010—29th International Congress on Applications of Lasers & Electro-Optics, Anaheim, CA, USA, 26–30 September 2010; pp. 225–232.
26. Schuster, J. *Heißrisse in Schweißverbindungen—Entstehung, Nachweis und Vermeidung*; DVS-Berich 233; DVS-Verlag: Düsseldorf, Germany, 2004.
27. Lampa, C.; Kaplan, A.F.H.; Powell, J.; Magnusson, C. An analytical thermodynamic model of laser welding. *J. Phys. D* **1997**, *30*, 1293–1299. [CrossRef]
28. Rahman Chukkan, J.; Vasudevan, M.; Muthukumaran, S.; Ravi Kumar, R.; Chandrasekhar, N. Simulation of laser butt welding of AISI 316L stainless steel sheet using various heat sources and experimental validation. *J. Mater. Process. Technol.* **2015**, *219*, 48–59. [CrossRef]
29. Kumar, S.; Kundu, A.; Venkata, K.A.; Evans, A.; Truman, C.E.; Francis, J.A.; Bhanumurthy, K.; Bouchard, P.J.; Dey, G.K. Residual stresses in laser welded ASTM A387 Grade 91 steel plates. *Mater. Sci. Eng. A* **2013**, *575*, 160–168. [CrossRef]
30. Dal, M.; Fabbro, R. An overview of the state of art in laser welding simulation. *Opt. Laser Technol.* **2015**, *78*, 1–13. [CrossRef]
31. Cross, C.E. On the Origin of Weld Solidification Cracking. In *Hot Cracking Phenomena in Welds*; Springer: Berlin, Germany, 2005; pp. 3–18.